πFBG resonator used as a transducer for trace gas photothermal detection

Thomas Lauwers, Alain Glière, Thierry Verdot, Skandar Basrour

Research Article | Vol. 29, No. 20 / 27 Sep 2021 / Optics Express 31796
Optics EXPRESS

πFBG resonator used as a transducer for trace gas photothermal detection

THOMAS LAUWERS,[1,*] ALAIN GLIÈRE,[1] THIERRY VERDOT,[1] AND SKANDAR BASROUR[2]

[1] *Université Grenoble Alpes, CEA, LETI, F38000 Grenoble, France*
[2] *Université Grenoble Alpes, CNRS, Grenoble INP†, TIMA, 38000 Grenoble, France*
[*] *thomas-lauwers@hotmail.fr*
[†] Institute of Engineering Univ. Grenoble Alpes

Abstract: We present an optical transduction method adapted to the detection of low frequency thermal perturbations and implemented for photothermal trace gas detection. The transducer is a π-phase shifted fiber Bragg grating, stabilized and interrogated by the Pound-Drever-Hall method. The principle of detection is based on the frequency shift of the narrow optical resonance, induced by the temperature variations. In temperature measurement mode, the stabilization leads to an estimated limit of detection of 1 µK at room temperature and at a frequency of 40 Hz. When the fiber transducer is placed in a gas cell, CO_2 is detected by photothermal spectroscopy with a limit of detection of 3 ppm/$\sqrt{\text{Hz}}$. This novel method, based on a single fiber, offers robustness, stabilized operation and remote detection capability.

1. Introduction

The photoacoustic or photothermal spectroscopy (PAS or PTS) is a well known method, used for trace gas detection. The method is based on the indirect measurement of the absorbed light, released by the gas in the form of heat or pressure wave. While PAS is widely used for trace gas detection and frequently based on electrical transduction techniques, photothermal trace gas detection essentially relies on optical transducers. In the next paragraphs, we focus on the latter techniques.

The traditional method for photothermal detection is based on the mirage effect. In this technique, the light beam of the probe laser is directly deviated by a refractive index variation due to a temperature change and measured with a position photodetector. This technique was implemented for photothermal spectroscopy [1–3] and showed a noise equivalent absorption of 10^{-7} cm^{-1} for methane in nitrogen. This technique has the advantage of using broadband sources, cheaper than narrow bandwidth lasers. However, the implementation is complicated as it requires an accurate optical alignment. Also, the remote detection capability is limited since this deflection technique requires a position photodetector placed in the vicinity of the gas sample.

A second category of optical transducers is based on interferometry. Here, the thermal perturbation induces a phase change of the propagating light which can be measured with an interferometric system. Highly reflective Fabry-Perot cavities were implemented [4,5], and showed high sensitivities with normalized noise equivalent absorptions (NNEA) of 10^{-6} and 10^{-7} W $\cdot$ cm$^{-1}\cdot$ Hz $^{-1/2}$.

In the last years, all-fibered interferometers coupled to hollow core fibers gained a lot of attention and reached record limit of detection (LOD), with increased robustness and compacity, and no need for a specific alignment compared to free-space interferometers. Such systems can be based on the Mach-Zehnder (MZI) or on the Fabry-Perot interferometers. In the MZI configuration, the sensing arm is an hollow core fiber filled with the target gas. The hollow core fiber is illuminated by the excitation and the probe light beam, helping to obtain a direct photothermal generation inside the fiber [6]. In this way, the MZI serves at the same time as

#437710 https://doi.org/10.1364/OE.437710
Journal © 2021 Received 14 Jul 2021; revised 19 Aug 2021; accepted 19 Aug 2021; published 20 Sep 2021

Optics EXPRESS

the gas cell and sensing element for PTS. The use of a hollow core fiber permits to achieve extremely small volumes of gas (the typical fiber diameter is of 10 μm) which are favorable to the generation of a photothermal wave at high frequencies, while reaching record lengths of 10 meters [7]. Consequently, very low NNEA can be reached with this technique of $\sim 10^{-7}$ [6] and $\sim 10^{-9}$ [7]. The use of long arms however makes the interferometer sensitive to thermal drift, and a piezo control must be added on the reference arm to compensate for these low frequency variations, leading to an increased complexity of the sensor. The use of a hollow core fiber inside the Fabry-Perot (FP) interfererometer was also demonstrated for PTS [8], [9] and enabled to reach NNEA of $\sim 10^{-7}$. In this configuration, both the excitation and probe light circulate in the FP cavity. For this reason, the FP resonance must be tuned to the target gas absorption line. The drawback of this system is that multi–gas operation is complicated, as the target gas depends not only on the excitation laser operating wavelength, but also on the FP cavity length.

In this article, we present a novel technique for photothermal detection, based on a fibered FP cavity. Contrary to the previously presented systems based on hollow core fibers, our cavity uses a compact fiber Bragg grating with a π-phase shift defect at its middle, called πFBG [10]. Such cavities are fabricated today on different materials such a silica [11] or for example polymers [12]. The proposed cavity, composed of a single glass fiber, is thus extremely robust. A photothermal wave is then generated outside the fibered optical cavity, and causes a temperature change inside the fiber by thermal conduction, creating a shift of the Fabry-Perot resonance. The optical resonator is interrogated by means of a specific technique based on the Pound-Drever-Hall locking, enabling to get rid of low frequency perturbations, and leading to a high sensitivity. The paper is structured into three sections, starting with the conception of the sensor, then the fabrication and experimental implementation, and finally the results and discussion.

2. Theoretical description

In this section, we describe the theoretical response of the whole sensor. The optical sensitivity, corresponding to the wavelength shift caused by a given photothermal perturbation is first calculated. Then, the photothermal frequency response is predicted using a transmission line model. Finally, the interrogation technique is studied, and some key parameters are considered for the sensor fabrication.

2.1. Optical sensitivity of the fiber Bragg grating cavity

The πFBG shows a narrow resonance at a specific wavelength, called Bragg wavelength λ_B. The resonance condition, given by $\lambda_B = 2n_e\Lambda$, depends on the effective refractive index of the fiber n_e and on the grating pitch Λ of the grating. Considering this expression, it appears that two main effects can cause a shift of the resonance frequency: the strain perturbation and the thermal perturbation.

Firstly, the strain perturbation induces a physical elongation of the fiber, causing a change of the grating pitch of $\delta\Lambda$, or a change of the fiber index δn_e due to the photoelastic effect. Secondly, the thermal perturbation causes a change of the grating period due to the thermal expansion of the fiber (mainly made of silica), or a change of the refractive index, which depends on the temperature. Considering these four contributions, Kersey et al. proposed [13] an expression of the Bragg wavelength shift for a given strain or thermal perturbation. The strain response is mainly dominated by the elongation of the structure ($\sim 78\%$) while the photoelastic effect remains weaker and opposed (minus sign) to this first contribution. Regarding the thermal response, the dn/dT effect accounts for $\sim 95\%$ of the wavelength shift. These sensitivities are expressed in term of a wavelength shift, usually a few picometers, per unit of temperature or strain. At the Bragg wavelength and at constant strain, the calculated value of the Bragg shift is 10.3 pm/K, while at constant temperature, it is 1.2 pm/$\mu\varepsilon$.

Optics EXPRESS

In the most simple configuration, we can assume that the fiber is freely suspended and has no contact with any mechanical vibrating element, and is thus only sensitive to the surrounding pressure. Under isotropic stress, the pressure induced strain is given by [14]:

$$\varepsilon = \varepsilon_z = -p\frac{1-2\nu}{E} \tag{1}$$

where p is the pressure, E is the Young modulus of the fiber material and ν its Poisson coefficient. The considered material is silica ($\nu = 0.17$ and $E = 70$ GPa), and the pressure is assumed to be uniformly distributed. Consequently, the resulting resonance shift can be expressed as a function of the pressure or temperature. The optical sensitivity is expressed in Table 1. Since the measured shift can be well below the picometer range, it is convenient for our application to rather express the wavelength shift $\delta\lambda_B$ in term of its equivalent frequency shift $\delta\nu_B$ in Hz, given by $\delta\nu_B = c_0/\lambda_0^2\delta\lambda_B$.

Table 1. Optical sensitivity of the FBG in the acoustic or thermal configuration at 1.55 μm

Optical sensitivity at 1.55 μm	Wavelength shift	Frequency shift
At constant temperature	1.3×10^{-7} pm/Pa	16 Hz/Pa
At constant pressure	10.3 pm/K	1.29 GHz/K

We observe that the pressure induced frequency shift has a much lower amplitude than the temperature induced frequency shift. Therefore, we expect a weak acoustic sensitivity for our transducer. In order to confirm this hypothesis, it is necessary to assess the photoacoustic and photothermal fields to obtain the typical wavelength shift expected for the gas sensing application in the photoacoustic (PA) or photothermal (PT) configuration. The next section is dedicated to the description of the transmission line model used for the PA and PT effect in the πFBG based sensor.

2.2. Photothermal generation in a cylindrical cell

The transducer consists of a single optical fiber, embedded in a cylindrical gas cell, whose walls are assumed to be rigid and isothermal. Moreover, we consider the absence of optical fiber inside the gas cell for the calculation of the thermal and pressure fields. The cell is subjected to a longitudinal illumination, causing a harmonic heat generation by optical absorption. Due to the aspect ratio of the considered cylindrical cell (long cylinder with a small diameter), and the optical absorption along the cell, a non uniform pressure distribution along the cell must be accounted for. Therefore, a solution consists in dividing the conduit into N small elements, with $N + 1$ pressure nodes (see Fig. 1, top). This approach, presented by Miklos et al. [15], considers an acoustic waveguide with an input $(p_n, \Delta i_n)$ and an output $(p_{n+1}, \Delta i_{n+1})$, where p indicates the acoustic pressure field and Δi the gas volume flow rate induced by pressure fluctuations arising between two sucessive nodes. Using this approach, the transfer function can be described by means of lumped elements which are the thermal admittance, denoted Y_{th} in this article, and the viscous impedance, denoted Z_v. For a complete description of the impedance and admittance terms, the reader may refer to the PhD thesis [16] and the work of Bruneau [17], Kampinga [18] and Benade [19]. This formalism, developed in the article from Miklos [15] allows electroacoustical analogies and provides two equivalent circuits (T and Π circuits in Fig. 1) that can be used for the description of a pipe as an acoustic waveguide. With this model, a pressure node can be electrically represented by a circuit in a T configuration (Fig. 1, left), and the small volume between two nodes can be represented with a circuit in the Π configuration (Fig. 1, right). In these representations, the photothermal generation has been taken into account using an additional photothermal volume flow rate i_n corresponding to the volume expansion caused by the deposited optical power in the considered element.

Optics EXPRESS

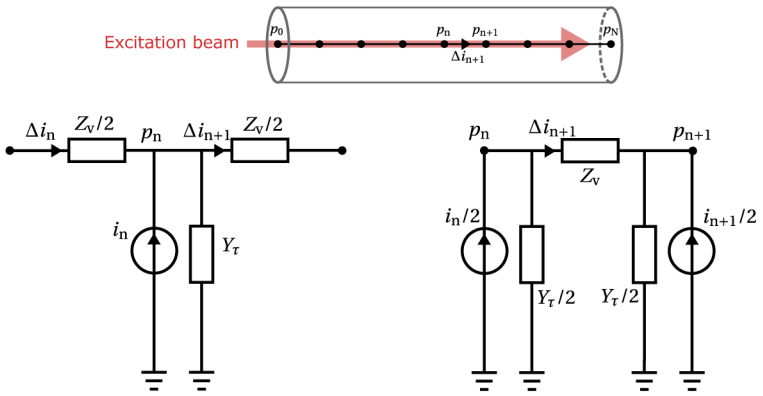

Fig. 1. T and Π conduit configuration

We note here that the lumped element model can be used only in the "low frequency" approximation, where the thermoviscous wavenumber k_ℓ is negligible compared to the inverse of the conduit length L ($|k_\ell L| \ll 1$). As a consequence, the system's response can be evaluated at any frequencies, if the considered conduit portion is short enough. A system of equations can be expressed while keeping the pressure fluctuations of the nodes as state variables. Given the photothermal volume rate flow, the system is solved to determine the pressure fluctuation in the waveguide. Once the pressure field is known, the temperature can be expressed using the Fourier law.

In the case of an enclosed volume of length dz with a deposited power H_n [W/m^3], the photothermal volumic expansion rate source i_n can be expressed, by considering an uniform pressure distribution [17,20]. Following the model of Fig. 1, the photothermal volumic expansion rate on each nodes can then be calculated. The amount of deposited power per unit of volume H_n in the small element at the n^{th} pressure node is calculated considering the Beer-Lambert absorption law. For an incident power of P_0 and a coefficient of absorption α, the deposited power in the n^{th} small element situated at z_n of section S is given by the expression:

$$H_n = -\frac{1}{S}\frac{dP}{dz}(z_n) = \frac{\alpha P_0}{S} e^{-\alpha z_n} \tag{2}$$

The acoustic transfer function for each node n is then described by the pressure increase p_n for an incident power P_0: $T_n^{\text{ac}}(\omega) = p_n/P_0$ [Pa/mW]. The thermal transfer can be calculated as well, and relates the temperature increase τ_n at the node n and the incident power: $T_n^{\text{th}}(\omega) = \tau_n/P_0$ [K/mW]. We calculate and show on Fig. 2 the acoustic and thermal transfer functions at the central node of a cylinder of radius 1 mm and length of 60 mm. To obtain a reliable response at high frequencies (10 kHz), the resolution is made with 11 nodes. When looking at the central node ($n = 5$), an odd number is preferred in order to have the same number of nodes before and after the central node.

We observe a perfect superposition of the transmission line model (black dotted line) with respect to the finite element method (FEM) resolution (blue continuous line) performed with a 2D axisymmetric geometry. The photoacoustic response is a low pass, with however an acoustic resonance in the kHz range, due to the non-uniform heat power distribution $H(z)$. The thermal response follows the pressure variation with the same cut-off frequency, with a plateau at $\sim$ 30 mK/mW. The plateau obtained for the PA response is of $\sim$ 5 Pa/mW.

Some concluding observations can be made with respect to these results. Firstly, considering Table 1, the generated pressure would lead to an extremely weak frequency shift compared to the thermal induced frequency shift. We therefore expect a negligeable contribution of the PA wave

Optics EXPRESS

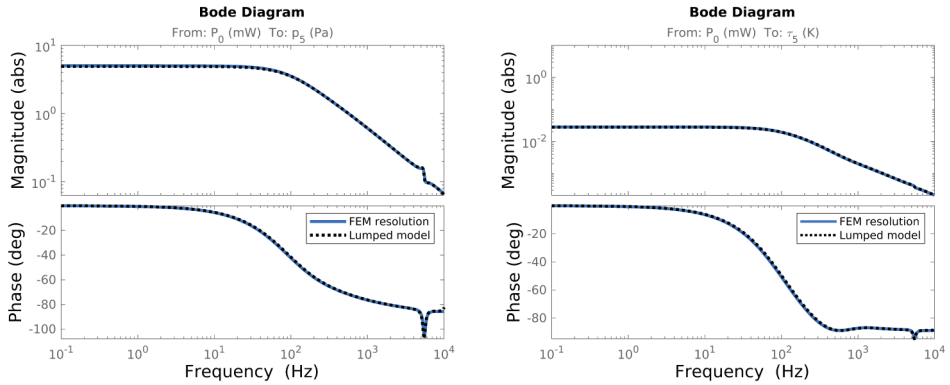

Fig. 2. Transfer function of the pressure and thermal field at the center of a 60 mm long cell with a radius of 1 mm, calculated with the lumped model (black dotted line) and the FEM (blue continuous line)

on the induced frequency shift. Secondly, the photothermal response has a low-pass response, meaning that the interrogation system must correctly operate at low frequencies, below 100 Hz. Finally, the calculations also showed an increase of the cut-off frequency for small volumes. Since working at higher frequencies partially reduces the noise, and in particular the noise induced by the whole measurement chain (e.g., the stabilization stage), small volumes are preferred.

These values therefore confirm that the designed transducer is adapted for photothermal detection, and also demonstrate how small the optical frequency is shifted (well below the picometer). Moreover, since the expected signal is maximised in the low frequency regime, a high noise is also expected in this region. This raises the question of an interrogation technique capable of reducing the low frequency fluctuations and able to detect such weak frequency shifts. In the following section, we present a powerful interrogation technique particularly adapted to our problem, based on the Pound-Drever-Hall (PDH) method.

2.3. Interrogation using the Pound-Drever-Hall stabilization

The Pound-Drever-Hall (PDH) method is a stabilization technique generally used to improve the laser frequency stability using an optical resonator as a reference [21]. Similarly, assuming a stable laser frequency operation, this method can be exploited to track the resonance shift of an optical resonator. The latter method was for example implemented to detect the strain occuring inside a πFBG [22], reaching a limit of detection lying in the picostrain range.

To track the resonance peak, a measurement of the detuning between the laser frequency and the optical resonance frequency is first performed, through the so-called "error signal". The error signal is proportional to the detuning, and can be fedback to the laser controller, in order to adjust the emission wavelength and keep a zero detuning. When the feedback is activated, the laser is "locked" onto the optical cavity resonance.

To generate the PDH error signal, the incident laser light is first phase (or frequency) modulated, and sent into the Fabry-Perot cavity. The reflected light is measured with a photodiode, and mixed at the modulation frequency (1f scheme), leading to the error signal, proportional to the derivative of the Fabry-Perot reflectivity. Optionally, the retrieved signal can be mixed at twice the modulation frequency (2f scheme), resulting in a signal proportional to the second derivative of the reflectivity spectrum. Contrary to the PDH technique which is a "top-of-fringe" locking technique, the 2f scheme enables quadrature locking [23].

Optics EXPRESS

In the case of 1f detection, the error signal can be analytically calculated [21] and expressed as a complex function χ:

$$\chi(\omega) = r(\omega)r^*(\omega + \Omega) - r^*(\omega)r(\omega - \Omega) \tag{3}$$

where ω indicates the frequency of the propagating light, Ω the modulation frequency, r the complex reflection coefficient of the Fabry-Perot cavity, and where * denotes the complex conjugate. Experimentally, the real part of χ is proportional to the in-phase component of the demodulated signal (generally denoted X in lock-in amplifiers), while the imaginary part corresponds to the quadrature component (denoted Y). Figure 3 shows the evolution of the χ function as a function of the detuning for three different modulation frequencies. As can be seen, the component maximizing the error signal slope at resonance depends on the modulation frequency: in the low frequency regime the modulation frequency lies well below the full width at half maximum (FWHM), the real part shows a larger slope, while in the high frequency regime ($\Omega >$ FWHM), the imaginary part should be considered. A greater slope is thus preferred, as it corresponds to an increase the optical sensitivity. When looking at the evolution of the error signal slope at resonance (see Fig. 3, bottom), it is clear that the imaginary part of the χ function shows a larger sensitivity in the high frequency regime. Another way of maximizing the error signal slope is obtained by reducing the FWHM of the optical resonator, that is in general obtained by increasing the grating length.

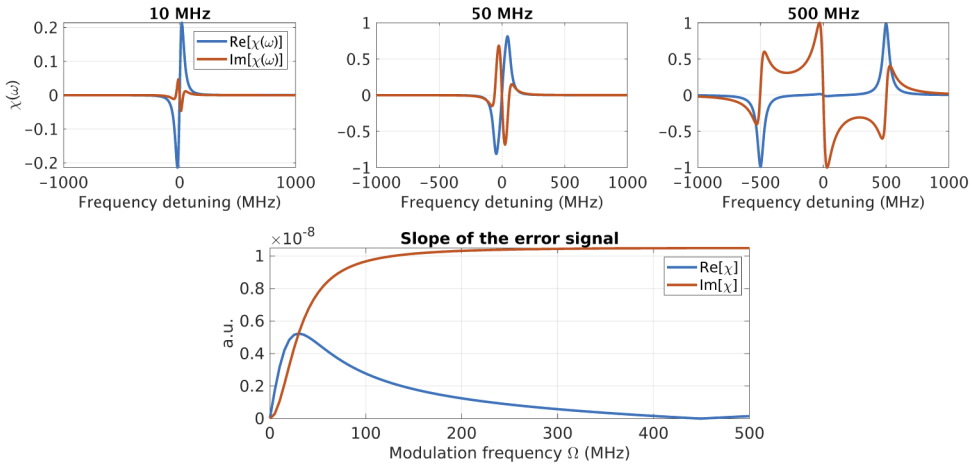

Fig. 3. At the top, complex error signal component after a reflection on a πFBG with a FWHM of 60 MHz, with various modulation frequencies (from left to right): Ω = 10, 50, 500 MHz. At the bottom, evolution of the error signal slope as a function of the modulation frequency Ω.

After low-pass filtering, the error signal can be measured and fedback to the laser through a PID controller. The PID stage helps to maintain the error signal to zero despite thermal drift or external vibrations, by controlling the laser wavelength. The PID stage is necessary to set a correct gain, as well as the desired feedback speed. This feedback is generally performed on the piezo voltage of an external cavity diode laser, enabling a fine tuning of the wavelength, with a resolution well below the picometer.

As a conclusion to the theoretical study, some considerations must be taken into account to increase the sensitivity and the signal-to-noise ratio. Firstly, the sensitivity of the PDH locking can be increased with a high modulation frequency Ω, and a narrow optical resonance, as they cause an increase of the slope of the error signal. A narrow resonance comes in general with a long fiber grating. Secondly, the amplitude of the photothermal wave can be increased with a

Optics EXPRESS

small volume, which leads to a higher thermal cut-off frequency. This consideration however implies the use of a small fiber grating to fit inside the volume, which is in contradiction with the first point. A first solution to this trade-off consists in minimizing the gas cell by using a cylindrical cell with a diameter equal or close to the fiber diameter, and a length equal to the grating length. Finally, the noise can be reduced, by chosing a high photothermal frequency ω_{PT}. The frequency ω_{PT} should however lie before the cut-off frequency of the thermal low-pass filter.

3. Sensor fabrication and caracterization set-up

The study presented above allowed us to evaluate the key design parameters for the sensor fabrication and the instrumentation bench, which we present in this part.

3.1. πFBG transducer and gas cell

The πFBG fabrication technique is based on the optical writing of a refractive index modulation inside the core of the fiber, and was first proposed by Hill et al. in 1978 [10]. To inscribe a spatial variation of the refractive index along the fiber, a grating is used as a diffractive element, called a phase mask, to produce an interference pattern. This interference technique can be used to produce a πFBG with a high quality resonance. An UV laser beam is focused in the fiber core and scanned along the first half of the πFBG. Then, the phase mask is translated by a distance $\Lambda/2$ with a nanopositioner to create the cavity defect. The UV laser is scanned again along the second part of the grating to produce finally two FBGs separated by Λ [24]. Another method consists in directly inserting a phase default on the mask to generate the π phase shift of the πFBG. The Bragg gratings used in the experiments presented in this paper have been fabricated by the *Laboratoire Capteurs Fibres Optiques*, from the LIST institute (CEA Saclay). For the following, two πFBG are considered, each of them showing a π defect situated at the center: a long grating, with a length of 40 mm and a FWHM of 0.6 pm, and a short grating of 10 mm length with a FWHM of 1.1 pm.

To perform a trace gas measurement, the Bragg transducer is placed in a gas cell, which is the second element of the sensor. The gas cell geometry is important, because we need, at the same time, a long interacting path between the absorbing gas and the light beam and a small volume to increase the photothermal generation. In order to keep a small volume, a cylindrical gas cell is chosen, with an illumination parallel to the fiber, and an as small as possible diameter. Two versions were proposed and fabricated: the first prototype is made by 3D printing and has large dimensions to allow an easy installation of the 40 mm long fiber transducer. In contrast, the second cell is more challenging to install, as it has the minimal acceptable size to let enter the 10 mm long fibered transducer.

The first gas cell prototype is 3D printed by means of a UV stereolytography technique, with the Form 2 printer (Formlabs). The material is a photosensitive black resin, cured with an ultraviolet source. Figure 4, top, shows the fabricated cell, composed of a 3D–printed cylindrical gas chamber and two adapters (each composed of a fiber chuck and a chuck holder), screwed together. The chuck holder embeds a commercially available fiber chuck, which enables a good mechanical holding without damaging the probe fiber (green arrow). A hole with a diameter of 1 mm is made in the chuck holder to let enter the excitation light (denoted with the red arrow). To have a reduced gas volume, the gas cell is a cylinder with an elliptical section (represented in the left upper inset): the upper focal point of the ellipse corresponds to the area excited by the light beam, while the lower focus matches with the location of the probe fiber. The distance between the ellipse foci must be larger than the radius of the fiber chuck of 5 mm (represented by the dotted circle in the inset).

To further reduce the gas cell volume, a second prototype is proposed, where the fiber chuck is removed, and the excitation light is brought by an optical fiber. The fiber used for the excitation is a indium fluoride fiber for single mode operation with a core diameter of 9 µm, a cladding

Optics EXPRESS

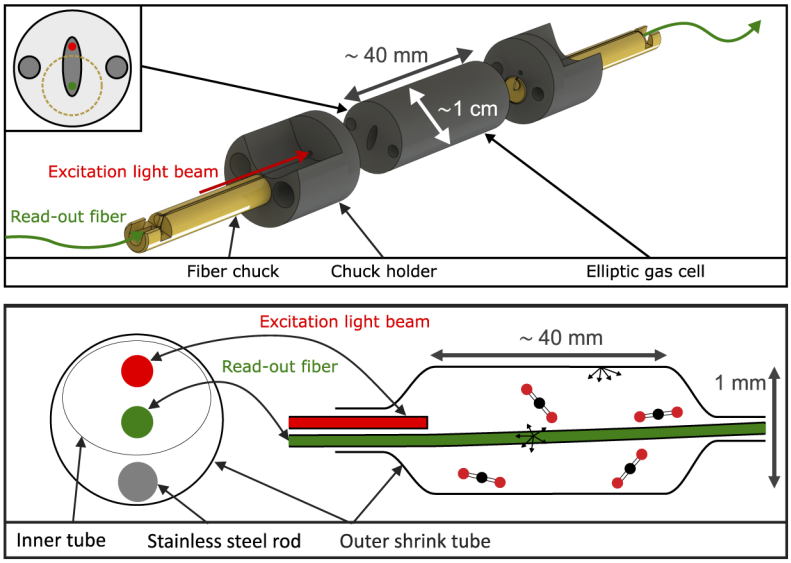

Fig. 4. Assembly of the πFBG based photothermal sensor: 3D printed cell configuration (top) and all fibered configuration (bottom)

of 125 µm and low optical loss (<0.5 dB) in the mid-IR range. In this way, the radius of the gas cell is only limited by the radius of both fibers (excitation and probe fiber). To build such a small chamber, the fibers are placed in a fiber sleeve with a diameter of 1 mm, and a length of 40 mm. The sleeve consists in a heat-shrinkable plastic tube, put together with a stainless steel rod that provides rigid support (see Fig. 4, bottom). Once the fiber is placed inside the sleeve, the two ends are heated to shrink the plastic tube and to hold the fibers together in the tube. Closing in this way the cell should also increase the low frequency PT signal and most importantly reduce the external noise by isolating the fiber grating from the external environment. However, we expect a high background signal, as the light beam is not collimated (fiber NA of 0.26) and the cell diameter is quite small compared to the 3D printed cell. The background signal, indicated by the black arrows on the walls, can come from the non specific photothermal generation originating from the cell wall absorption, but also from the temperature increase due to the direct excitation of the read-out fiber (indicated by the black arrows on the fiber).

3.2. *Caracterization bench*

The detection scheme for photothermal detection with the πFBG is shown on Fig. 5. The excitation laser (red light beam) is a Quantum Cascade Laser (AdTech). The light beam is launched into the gas cell and is wavelength modulated at a low frequency ω_{PT} to excite the gas and generate a photothermal wave. Simultaneously, the laser wavelength is slowly moved to scan the entire absorption peak spectrum. For the photothermal reading, the probe laser light (DL pro, Toptica) is launched into the fiber transducer (green light beam), and the light phase is modulated with an electro-optic modulator (iXBlue, MPX-LN-0.1, 150 MHz Bandwidth) at Ω, in the MHz range, to perform the PDH locking.

Then, the reflected light is measured by the photodetector and demodulated at two frequencies. This is the main peculiarity of this detection scheme, that requires two lock-in inputs (one is used for the stabilization, the other for the signal detection):

- A first channel is used for the laser frequency tracking (PDH method) and compensates the thermal drift and noise fluctuations of the πFBG resonance. This channel mixes the

Optics EXPRESS

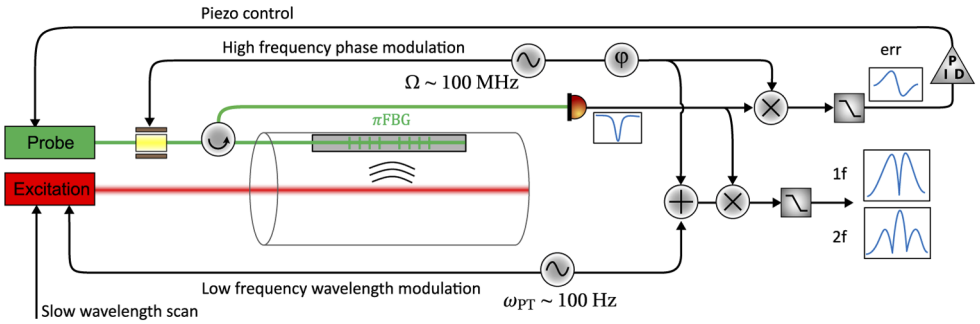

Fig. 5. πFBG photothermal trace gas detection bench

photodetector signal with the reference phase modulation signal at frequency Ω and a low pass filter is applied to generate the error signal. A phase shift φ is added to compensate for the phase delays in the circuit and select the quadrature component of the error signal, where the slope at resonance is maximised. This signal is fed back to the laser piezo voltage, after a PID stage.

- A second channel channel is used for the detection of the photothermal perturbation. This channel mixes the photodetector signal with a signal oscillating at $\Omega + n\omega_{PT}$, at the first harmonic (1f scheme, $n = 1$) or second harmonic (2f scheme, $n = 2$).

The two fabricated cells are installed on the same bench. To illuminate either one or the other cell, the excitation laser is placed on an optical rail and focusing lenses are used to couple the laser light into the cells. For the 3D printed cell, a lens with a focal length of 150 mm is placed in front of the cell. The second lens has a focal length of 11 mm and is placed on a five degrees of freedom platform (X,Y and tilt) to align the laser spot into the optical fiber. The fiber, made of indium fluoride glass shows a transmission of ~ 95%/m at the operating wavelength of 4.2 µm.

4. Experimental results

4.1. Frequency stabilization

The two πFBG spectra, respectively centered around 1530.7 nm for the 40 mm sample and 1530.9 nm for the 10 mm sample, are tested. Both show a narrow resonance at the Bragg wavelength situated in the middle of the reflectivity profile. To study these optical resonators, the external cavity diode laser is used. After a coarse positioning of the laser wavelength, a fine tuning of the wavelength is performed with the piezo controller in order to center the Bragg resonance. Then, a triangular scan of the piezo voltage is applied to scan the entire cavity response, given by the DC component of the reflected power. In the meantime, the phase is modulated at the frequency Ω and the phase offset φ is adjusted to provide a zero phase on the error signal at resonance, with a 180° phase jump. Once the correct phase offset φ is found, the experimental parameters are saved: piezo voltage at resonance, cavity FWHM and slope of the error signal. These parameters are necessary to calculate the ideal PID parameters for the closed-loop operation.

The cavity response and error signal is measured for the two πFBGs. As expected, the 40 mm grating shows a narrowest bandwidth of 0.6 pm (equivalent to 80 MHz) while the 10 mm grating has a bandwidth of 1.1 pm (equivalent to 142 MHz). Consequently, the narrow grating has a higher error slope of 58.2 mV/pm, versus 9.6 mV/pm for the shorter one. Here, the modulation frequency is fixed to 10 MHz, in order to stay in a low frequency regime ($\Omega \ll$ FWHM). We note that the length of the optical resonator has a direct impact on its bandwidth (or FWHM) and thus on its sensitivity. This lead us to the trade-off mentioned in the conclusion of the theoretical

Optics EXPRESS

description: to increase the optical sensitivity a long resonator is preferred, but at the same time a small gas volume is needed to increase the photothermal generation. The second sample has a length of 10 mm and a FWHM of 142 MHz and thus offers a good compromise between a narrow cavity resonance and a compact resonator. It will thus become the reference sample for the current study, focused on the optimization of the PDH technique.

Figure 6 shows the error signal obtained for the 10 mm long grating for two frequencies. After a frequency analysis, the optimal frequency of $\Omega = 125$ MHz is chosen (left), as it approaches the high frequency regime ($\Omega \gtrsim$ FWHM), while staying below the photodetector and modulator cut-off frequency. For example, if $\Omega = 300$ MHz is chosen, the PD and EOM cut-off lead to a decrease of the signal (right).

For the closed-loop operation, the piezo voltage scan is deactivated (see Fig. 7, at $t = -14$ s) and the voltage is slowly adjusted near resonance (from $t = -14$ s to 0 s). Once the resonance is approximately reached — i.e. the cavity response starts to decrease —, the analog control of the laser piezo is activated, as well as the PID, at $t = 0$ s. We emphasize the importance of the coarse voltage adjustment before the activation of PID because it enables to ensure that the zero crossing point corresponds to the cavity resonance, and not to the sides, away from the resonance, where the error signal is also equal to zero. Provided a good tuning of the PID parameters, the system locks to the zero error signal after a few seconds. As shown on the upper curve presenting the cavity response, the zero error signal locking corresponds to the lowest reflectivity, i.e. to the optical resonance of the cavity.

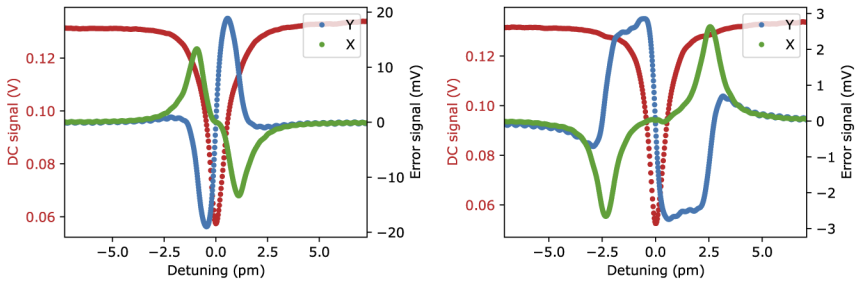

Fig. 6. Cavity and error signal for two modulation frequencies: $\Omega = 125$ MHz (left) and $\Omega = 300$ MHz (right). The drop of sensitivity after 125 MHz is due to the EOM cut-off (150 MHz) and the photodetector cut-off frequency (200 MHz)

The lock-in parameters must be carefully chosen for the closed loop operation. As in most applications, a Proportional-Integral (PI) controller is efficient to correct the environmental perturbations [25], so the derivative parameter is set to zero. The proportional parameter K_P is fixed by the inverse of the error signal slope. This term is expressed in V/V (piezo voltage per unit of error signal voltage) and corresponds to the piezo voltage correction that must be applied to correct a small variation of the error signal. The second parameter of importance is the integral term K_I which influences mainly the speed of the control loop. This term can be calculated in a first approximation by $K_I = \omega_c K_P$, where ω_c is the target bandwidth. Its value is fixed above the typical frequencies of the environmental noise, which is dominated by thermal drift, low frequency acoustic perturbations or mechanical vibrations. In addition, the πFBG transducer acoustic and thermal study showed that the signal of interest should rather originate from photothermal perturbations, with a maximized amplitude at low frequencies, below 100 Hz. We thus have a trade-off between the PI bandwidth ω_c and the signal of interest frequency. In other terms, the control-loop should reduce the low frequency noise, but should not cancel the signal of interest. As a consequence, the PI bandwidth must be chosen smaller than the photothermal signal frequency. Finally, the low pass filter, situated just before the PID, has also

Optics EXPRESS

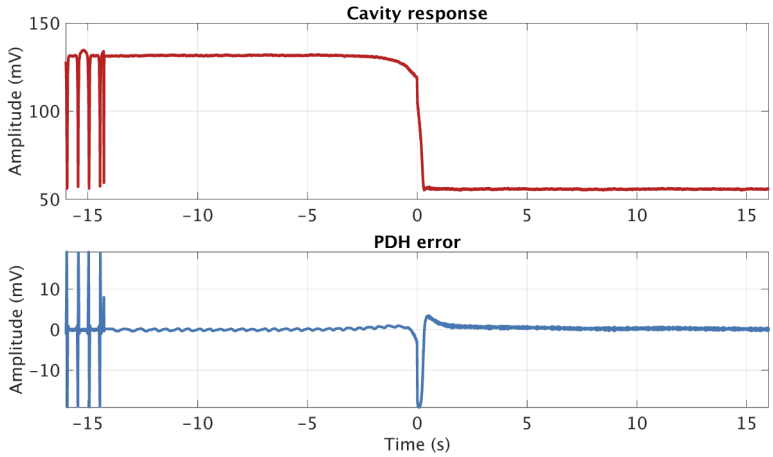

Fig. 7. Cavity scan for t<14 s, progressive step-by-step piezo setting, and PDH locking starting at $t \approx 0$ s, with a stabilized signal after a few seconds

an influence on the closed-loop operation. The filter cut-off is generally fixed higher than the PI cut-off frequency, in order to provide the maximum bandwidth to the PI controller (more details on the PID implementation can be found in the PhD thesis [16]).

A measurement of the noise spectrum of the error signal during the closed operation is performed (Fig. 8). The noise, expressed in $V/\sqrt{Hz}$, corresponds to the absolute value of the demodulated component at $\Omega + \omega_p$ normalized by the noise equivalent bandwidth.

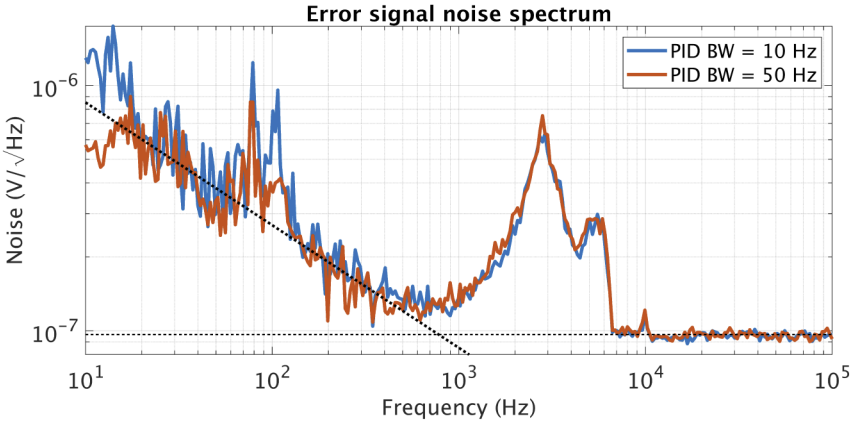

Fig. 8. Error signal noise spectrum for a 1 Hz NEP (noise equivalent bandwidth)

From this spectrum, three interesting areas can be highlighted. Firstly, from 10 Hz to approximately 1 kHz, we observe a low frequency noise proportional to $1/\sqrt{f}$. The spectrum with a PI bandwidth of 50 Hz shows a noise cancellation at low frequencies (from 10 to 50 Hz) while the 10 Hz PI bandwidth spectrum continues increasing. We observe also a noisy source from around 80 to 100 Hz, which is probably due to external mechanical perturbations acting on the fiber. Then, from 1 kHz to 7 kHz, a broad resonance is observed, and corresponds to the mechanical resonance of the laser piezo. Finally, after the piezo resonance, a floor of 96 $nV/\sqrt{Hz}$ is reached, corresponding to the ultimate measurable frequency shift. This frequency noise floor is attributed to the intrinsic laser linewidth, also called free running frequency noise.

Optics EXPRESS

Considering the measured voltage to frequency shift sensitivity of 58 mV/pm, a noise floor of 1.6×10^{-6} pm/$\sqrt{\text{Hz}}$ is calculated, which corresponds to a frequency noise of 205 Hz/$\sqrt{\text{Hz}}$ at 1530 nm. Assuming a Lorentzian lineshape with a white spectral density of frequency noise S_f, we can relate it to the linewidth of the laser $\Delta\nu$ ([26], [27], [28]) by $\Delta\nu = \pi S_f^2$. We find an intrinisc linewidth of 130 kHz, which fits with the approximative intrinsic linewidth of $\sim$ 100 kHz announced by the manufacturer. Considering the frequency noise (1σ) at the typical photothermal frequency of 40 Hz and the thermal sensitivity calculated in the previous section of 10.3 pm/K, the photothermal limit of detection (LOD) is calculated to be equal to 0.7 µK. We note that at higher frequencies however (above 100 Hz), this calculation is not valid anymore, as the thermal conduction inside the fiber cannot be considered to be immediate with respect to the operating frequency.

4.2. Trace gas photothermal spectroscopy

When the PDH locking is activated, the excitation source is focused into the cell and the QCL supply current is adjusted to excite the side of the target gas absorption peak (1f detection). For the gas sensing demonstration, carbon dioxide is selected as it provides a strong absorption line at 2362.8 cm^{-1}, directly in the laboratory atmosphere, without the need for any additional sampling device. In a first step, in order to identify the optimal working frequency ω_{PT}, a frequency scan is performed. The photothermal response of the 3D printed cell equipped with the 40 mm πFBG is measured for a control loop bandwidth of 10 Hz and three different low-pass filters (Fig. 9, left).

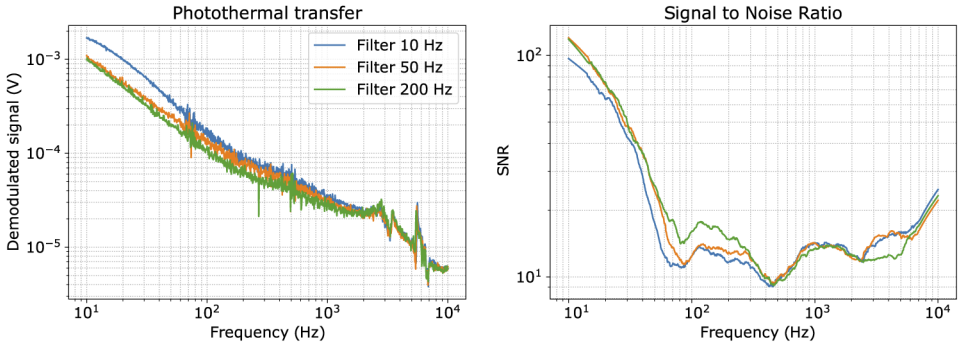

Fig. 9. Photothermal response of the 3D printed cell, for a PID bandwidth of 10 Hz and three different low pass filters

The typical low pass behavior predicted in section 2.2 for photothermal generation in a closed cylindrical cell is noticed. For low frequencies (<100 Hz), we observe an influence of the filter bandwidth: a higher filter bandwidth results in a correction of the photothermal perturbation, leading to a lower signal. At higher frequencies, from 2 kHz to 7 kHz, the laser piezo resonance that was already visible on the noise spectrum (Fig. 8). The signal to noise ratio, showed on the right plot, is also maximal at very low frequencies. However, since the noise is considerably reduced for high filters bandwidth (50 Hz or 200 Hz), the global SNR is increased to $\sim$ 110, despite a lower photothermal amplitude. After a few tens of Hz, the SNR exhibits a drop and keeps its lowest value ($\sim 10-20$) until the end of laser piezo resonance, where the system reaches its ultimate noise floor.

In the same way, the photothermal response is measured for the all – fibered gas cell (see Fig. 10), equipped with the 10 mm πFBG. Since the volume is much reduced, we expect a higher low pass cut-off frequency, of few tens of Hz. The measured SNR from Fig. 10 shows a plateau up to a certain frequency, that depends on the filter bandwidth. In this case, the optimum is obtained at a photothermal frequency of 40 Hz and with a filter bandwidth of 10 Hz, leading to a

Optics EXPRESS

SNR of ~ 150. In the kHz range, the piezo noise is still visible but not as important as in the first configuration. We can thus conclude that the photothermal signal is further away from the noise floor compared to the first cell.

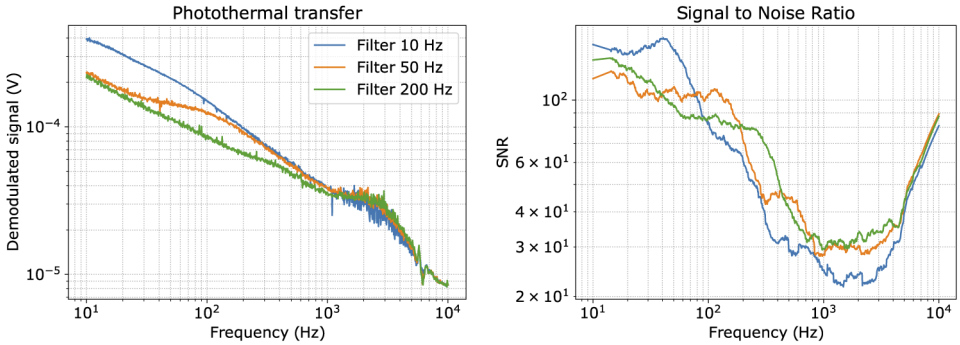

Fig. 10. Photothermal response of the all-fibered cell, for a PID bandwidth of 5 Hz and three different filter bandwidths

In a second step, a scan of the target gas absorption line is performed. The laser temperature is set to 25°C and the current is swept from 380 mA to 420 mA. In this wavelength region, the laser scans the atmospheric CO_2 absorption peak situated at 2362.8 cm^{-1}. For the 3D printed cell, the laser current is modulated with a depth of 5 mA (corresponding to 0.12 cm^{-1}) at a frequency of 10 Hz. The resulting 1f and 2f scans are presented on Fig. 11(a).

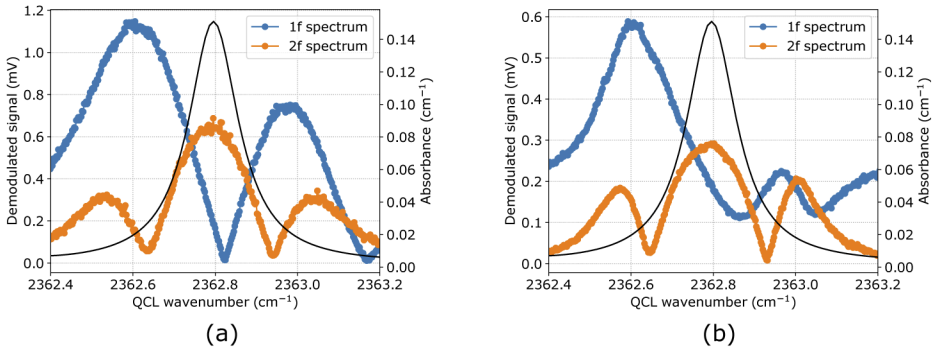

Fig. 11. Photothermal 1f and 2f spectra compared to the reference absorbance value for atmospheric CO_2 in the case of (a) the 3D printed cell and (b) the all-fibered cell

The blue curve is proportional to the first derivative of the absorption peak, with a maximal amplitude on the sides. Since the 1f-spectrum is sensitive to the background signal and the incident power, a 2f-spectrum (orange curve), is preferred. This signal is as expected proportional to the second derivative of the absorption peak, with a maximum value of 640 mV. Assuming a concentration of 400 ppm of CO_2 in the experiment room, this value leads to an approximate sensitivity of 1.6 µV/ppm. The Fig. 11(b) shows the photothermal spectrum obtained for the all-fibered cell.

The main difference with the previous spectra is the shape of the 1f spectrum, which is affected by to the presence of a strong background signal noise. The origin of this noise, already discussed in the fabrication section, can be explained by i) the generation of a photothermal signal originating from the cell walls absorption rather than from the target gas, and ii) the generation of a thermal perturbation inside the fiber, due to the direct excitation of the probe fiber that overlaps

Optics EXPRESS

with the excitation light beam. We note that the 2f detection scheme efficiently removes the background signal, making it appropriate for photothermal detection. The maximum value is here equal to 0.29 mV, leading to an approximate sensitivity of 0.7 µV/ppm.

4.3. Discussion

To provide more insights on the sensor performance for photothermal detection, the sensitivities obtained in the upper section have to be compared to the measured noise, and also to the amount of deposited power, which varies for the two gas cell configurations. For the 3D printed cell, the laser light crosses 15 cm of air before being coupled into the cell. Considering the CO_2 absorption and the emitted power of the laser at this wavelength, the incident power in the cell is of ~ 5 mW. For the all-fibered cell, the losses are also substantial (4 cm of air before reaching the fiber, and additional loss for the light beam coupling into the fiber), leading to an incident power estimated to ~ 15 mW. We summarize in Table 2 an assessment of the two cells sensitivities, LOD and NNEA, retrieved from the experimental measurements presented above. We recall that these values are an estimation, as they rely on approximate atmospheric CO_2 concentration.

Table 2. Performance of the πFBG sensor for CO_2 detection

	3D printed cell	All fibered cell
Volume (µL)	380	30
PT frequency (Hz)	10	40
Incident power (mW)	~ 5	~ 15
Sensitivity (µV/ppm)	~ 1.6	~ 0.7
SNR	~ 110	~ 150
$LOD_{1\sigma}$ (ppm/$\sqrt{\text{Hz}}$)	~ 3.4	~ 2.5
$NNEA_{1\sigma}$ (W · cm^{-1} · Hz $^{-1/2}$)	~ 6.4×10^{-6}	~ 1.4×10^{-5}

Firstly, it can be noticed that the NNEA is higher for the all-fibered system, despite a small cell volume. This higher NNEA is in part due to the reduced length of the πFBG, which results in a larger optical resonance of FWHM = 1.1 pm (instead of 0.6 pm for the 3D printed cell) and thus a lower optical sensitivity. Most importantly, the NNEA increase is mainly due to the divergence of the excitation fiber output inside the tiny 1 mm diameter gas cell. In addition, during the assembly — which consists of heating the fiber sleeve to enclose the two fibers (excitation and probe) in the small volume — the alignment cannot be controlled with accuracy. The result of this non optimized illumination is i) a shorter interaction length with the gas and thus a lower PT signal and ii) a strong background signal originating from unwanted probe fiber and walls illumination, contributing to a higher noise. The combination of these two effects produces a drop of the SNR and as a consequence a higher NNEA. These observations however could be further confirmed by a more precise model, which should take into account the exact boundary conditions at the cell walls (which, depending on the sensor architecture, are not perfectly isothermal or rigid) and the presence of the fiber transducer. Considering also the optical divergence of the excitation beam in the model could also help to evaluate the deposited power inside the gas cell.

The second observation concerns the absolute value of the NNEA, which is higher compared to other Fabry-Perot based PT sensors described in the literature: a lower NNEA of 1.8×10^{-6} W · cm^{-1} · Hz $^{-1/2}$ was reported [4], and more recently of 7.5×10^{-8} W · cm^{-1} · Hz $^{-1/2}$ was reached [5]. However, these results are obtained with free-space Fabry-Perot interferometers, and not with a completely guided interferometer like the πFBG transducer, which has many advantages (no alignment, compactness, robustness, etc.) compared to the free-space interferometer. Moreover, the presented results are meant to show the potential for this transducer, coupled with a Pound-Drever-Hall technique, rather than reach the highest possible sensitivity. Indeed, various

Optics EXPRESS

points for improvement can be put forward, like for example increasing the quality factor of the πFBG resonance, or decreasing the cell volume to work at higher photothermal frequencies where the noise is reduced. Moreover, the light injection inside the cell could be improved by the use of gradient index lenses in order to better focus the light beam and thus reduce the background signal.

5. Conclusion

To the best of our knowledge, we demonstrated the first application of fiber Bragg grating cavities, namely πFBGs, used as photothermal transducers for the detection of gas traces.

Based on a theoretical study of the optical sensitivity of the πFBG and the expected photothermal effect inside the cell, two πFBG based sensors have been designed, fabricated and characterized. A specific interrogation technique based on the Pound-Drever-Hall locking was implemented, and showed an excellent stability and thermal sensitivity, with an extremely low limit of detection in the µK range at room temperature and at a frequency of 40 Hz. The πFBG transducers were then implemented in two gas cell prototypes and submitted to a photothermal perturbation, originating from the strong atmospheric CO_2 absorption line at 2362.8 cm^{-1}. This first demonstration resulted in a sensitivity of 1.6 µV/ppm on a 3D printed cell, and a lower sensitivity of 0.7 µV/ppm on a fibered coupled cell. The NNEA obtained with the πFBG transducer is in the 10^{-6} W $\cdot$ $cm^{-1} \cdot$ Hz $^{-1/2}$ range.

To conclude, we want to point out the promising potential of the πFBG transducer used for photothermal detection. The transducer shows a high robustness, and no need for an optical alignment, since the high finesse cavity is directly fabricated inside the fiber. Moreover, contrary to hollow-core fiber systems, the proposed sensor configuration uses an excitation source situated outside the optical cavity, thus enabling multi–gas operation. We believe also that the demonstration of this πFBG transducer with its associated PDH locking technique paves the way towards miniaturization and remote sensing applications [29].

Aknowledgements. The authors would like to thank Guillaume Laffont and Romain Cotillard from CEA LIST (Saclay) for the fabrication of the fiber Bragg gratings, and Joris Baraillon, from CEA LETI (Grenoble), for providing his invaluable assistance on the PDH stabilization technique.

Disclosures. The authors declare no conflicts of interest.

Data availability. Data underlying the results presented in this paper are not publicly available at this time but may be obtained from the authors upon reasonable request.

References

1. B. L. Zimering and A. C. Boccara, "Applications of a compact photothermal-deflection-based setup for trace-gas detection in real-time in situ environmental monitoring and chemical analysis," Appl. Opt. **36**(15), 3188 (1997).
2. G. Leahu, R. L. Voti, S. Paoloni, C. Sibilia, and M. Bertolotti, "Trace gas analysis from glazes by means of a compact photothermal deflection spectroscopy apparatus," Rev. Sci. Instrum. **84**(12), 123111 (2013).
3. O. Dada and S. Bialkowski, "A Compact, Pulsed Infrared Laser-Excited Photothermal Deflection Spectrometer," Appl. Spectrosc. **65**(2), 201–205 (2011).
4. J. P. Waclawek, V. C. Bauer, H. Moser, and B. Lendl, "2f-wavelength modulation Fabry-Perot photothermal interferometry," Opt. Express **24**(25), 28958 (2016).
5. P. Breitegger, B. Lang, and A. Bergmann, "Intensity Modulated Photothermal Measurements of NO2 with a Compact Fiber-Coupled Fabry–Pérot Interferometer," Sensors **19**(15), 3341 (2019).
6. Z. Li, Z. Wang, F. Yang, W. Jin, and W. Ren, "Mid-infrared fiber-optic photothermal interferometry," Opt. Lett. **42**(18), 3718 (2017).
7. W. Jin, Y. Cao, F. Yang, and H. L. Ho, "Ultra-sensitive all-fibre photothermal spectroscopy with large dynamic range," Nat. Commun. **6**(1), 6767 (2015).
8. Y. Tan, W. Jin, F. Yang, Y. Jiang, and H. L. Ho, "Cavity-Enhanced Photothermal Gas Detection With a Hollow Fiber Fabry-Perot Absorption Cell," J. Lightwave Technol. **37**(17), 4222–4228 (2019).
9. F. Yang, Y. Tan, W. Jin, Y. Lin, Y. Qi, and H. L. Ho, "Hollow-core fiber Fabry–Perot photothermal gas sensor," Opt. Lett. **41**(13), 3025 (2016).
10. K. O. Hill, Y. Fujii, D. C. Johnson, and B. S. Kawasaki, "Photosensitivity in optical fiber waveguides: Application to reflection filter fabrication," Appl. Phys. Lett. **32**(10), 647–649 (1978).

Optics EXPRESS

11. K. O. Hill, B. Malo, F. Bilodeau, D. C. Johnson, and J. Albert, "Bragg gratings fabricated in monomode photosensitive optical fiber by UV exposure through a phase mask," Appl. Phys. Lett. **62**(10), 1035–1037 (1993).
12. C. Marques, A. Leal-Junior, R. Min, M. Domingues, C. Leitão, P. Antunes, B. Ortega, and P. André, "Advances on polymer optical fiber gratings using a krf pulsed laser system operating at 248 nm," Fibers **6**(1), 13 (2018).
13. A. D. Kersey, M. A. Davis, H. J. Patrick, M. LeBlanc, K. P. Koo, C. G. Askins, M. A. Putnam, and E. J. Friebele, "Fiber grating sensors," J. Lightwave Technol. **15**(8), 1442–1463 (1997).
14. G. B. Hocker, "Fiber-optic sensing of pressure and temperature," Appl. Opt. **18**(9), 1445–1448 (1979).
15. A. Miklós, P. Hess, and Z. Bozóki, "Application of acoustic resonators in photoacoustic trace gas analysis and metrology," Rev. Sci. Instrum. **72**(4), 1937–1955 (2001).
16. T. Lauwers, Optical transduction methods for the photoacoustic and photothermal detection of trace gas, Ph.D. thesis, Université Grenoble Alpes, Grenoble, France (2021).
17. M. Bruneau, Fundamentals of acoustics (Wiley-ISTE, Hawthorne, CA, United-States, 2006).
18. W. Kampinga, Viscothermal acoustics using finite elements: analysis tools for engineers, Ph.D. thesis, University of Twente, Enschede, The Netherlands (2010).
19. A. H. Benade, "On the propagation of sound waves in a cylindrical conduit," J. Acoust. Soc. Am. **44**(2), 616–623 (1968).
20. T. Lauwers, A. Gliére, and S. Basrour, "An all-optical photoacoustic sensor for the detection of trace gas," Sensors **20**(14), 3967 (2020).
21. E. D. Black, "An introduction to Pound–Drever–Hall laser frequency stabilization," Am. J. Phys. **69**(1), 79–87 (2001).
22. J. H. Chow, D. E. McClelland, M. B. Gray, and I. C. Littler, "Demonstration of a passive subpicostrain fiber strain sensor," Opt. Lett. **30**(15), 1923 (2005).
23. G. Liu and M. Han, "Wavelength Locking of a Diode Laser to the Maximal Slope of a π-Phase-Shifted Fiber Bragg Grating for Acoustic Emission Detection," IEEE Sens. J. **18**(22), 9257–9262 (2018).
24. Q. Zhang, N. Liu, T. Fink, H. Li, W. Peng, and M. Han, "Fiber-Optic Pressure Sensor Based on π-Phase-Shifted Fiber Bragg Grating on Side-Hole Fiber," IEEE Photonics Technol. Lett. **24**(17), 1519–1522 (2012).
25. X. Mao, S. Yuan, P. Zheng, and X. Wang, "Stabilized Fiber-Optic Fabry–Perot Acoustic Sensor Based on Improved Wavelength Tuning Technique," J. Lightwave Technol. **35**(11), 2311–2314 (2017).
26. B. Lissak, A. Arie, and M. Tur, "Highly sensitive dynamic strain measurements by locking lasers to fiber Bragg gratings," Opt. Lett. **23**(24), 1930 (1998).
27. T. C. Zhang, J. P. Poizat, P. Grelu, J. F. Roch, P. Grangier, F. Marin, A. Bramati, V. Jost, M. D. Levenson, and E. Giacobino, "Quantum noise of free-running and externally-stabilized laser diodes," Quantum Semiclassical Opt. **7**(4), 601–613 (1995).
28. J. Chow, I. Littler, G. de Vine, D. McClelland, and M. Gray, "Phase-sensitive interrogation of fiber Bragg grating resonators for sensing applications," J. Lightwave Technol. **23**(5), 1881–1889 (2005).
29. A. Rosenthal, M. Omar, H. Estrada, S. Kellnberger, D. Razansky, and V. Ntziachristos, "Embedded ultrasound sensor in a silicon-on-insulator photonic platform," Appl. Phys. Lett. **104**(2), 021116 (2014).